TISSUE ENGINEERING: Part A
Volume 26, Numbers 9 and 10, 2020

DOI: 10.1089/ten.tea.2019.0319

termis
Tissue Engineering
& Regenerative Medicine
International Society

ORIGINAL ARTICLE

Bioprinted Skin Recapitulates Normal Collagen Remodeling in Full-Thickness Wounds

Adam M. Jorgensen, BS,[1] Mathew Varkey, PhD,[1] Anastasiya Gorkun, PhD,[1–3] Cara Clouse, DVM,[1] Lei Xu, MD,[1] Zishuai Chou, BS,[1] Sean V. Murphy, PhD,[1] Joseph Molnar, MD, PhD,[1,4] Sang Jin Lee, PhD,[1] James J. Yoo, MD, PhD,[1] Shay Soker, PhD,[1] and Anthony Atala, MD[1]

Over 1 million burn injuries are treated annually in the United States, and current tissue engineered skin fails to meet the need for full-thickness replacement. Bioprinting technology has allowed fabrication of full-thickness skin and has demonstrated the ability to close full-thickness wounds. However, analysis of collagen remodeling in wounds treated with bioprinted skin has not been reported. The purpose of this study is to demonstrate the utility of bioprinted skin for epidermal barrier formation and normal collagen remodeling in full-thickness wounds. Human keratinocytes, melanocytes, fibroblasts, dermal microvascular endothelial cells, follicle dermal papilla cells, and adipocytes were suspended in fibrinogen bioink and bioprinted to form a tri-layer skin structure. Bioprinted skin was implanted onto 2.5×2.5 cm full-thickness excisional wounds on athymic mice, compared with wounds treated with hydrogel only or untreated wounds. Total wound closure, epithelialization, and contraction were quantified, and skin samples were harvested at 21 days for histology. Picrosirius red staining was used to quantify collagen fiber orientation, length, and width. Immunohistochemical (IHC) staining was performed to confirm epidermal barrier formation, dermal maturation, vascularity, and human cell integration. All bioprinted skin treated wounds closed by day 21, compared with open control wounds. Wound closure in bioprinted skin treated wounds was primarily due to epithelialization. In contrast, control hydrogel and untreated groups had sparse wound coverage and incomplete closure driven primarily by contraction. Picrosirius red staining confirmed a normal basket weave collagen organization in bioprinted skin-treated wounds compared with parallel collagen fibers in hydrogel only and untreated wounds. IHC staining at day 21 demonstrated the presence of human cells in the regenerated dermis, the formation of a stratified epidermis, dermal maturation, and blood vessel formation in bioprinted skin, none of which was present in control hydrogel treated wounds. Bioprinted skin accelerated full-thickness wound closure by promoting epidermal barrier formation, without increasing contraction. This healing process is associated with human cells from the bioprinted skin laying down a healthy, basket-weave collagen network. The remodeled skin is phenotypically similar to human skin and composed of a composite of graft and infiltrating host cells.

Keywords: skin, bioprinting, wound healing, animal models, extracellular matrix, tissue engineering

Impact Statement

We have demonstrated the ability of bioprinted skin to enhance closure of full-thickness wounds through epithelialization and normal collagen remodeling. To our knowledge, this article is the first to quantify collagen remodeling by bioprinted skin in full-thickness wounds. Our methods and results can be used to guide further investigation of collagen remodeling by tissue engineered skin products to improve ongoing and future bioprinting skin studies. Ultimately, our skin bioprinting technology could translate into a new treatment for full-thickness wounds in human patients with the ability to recapitulate normal collagen remodeling in full-thickness wounds.

[1]Wake Forest Institute for Regenerative Medicine, Wake Forest School of Medicine, Winston-Salem, North Carolina, USA.
[2]FSBSI Institute of General Pathology and Pathophysiology, Moscow, Russia.
[3]Institute for Regenerative Medicine, Sechenov First Moscow State Medical University, Moscow, Russia.
[4]Department of Plastic and Reconstructive Surgery, Wake Forest University Baptist Medical Center, Winston-Salem, North Carolina, USA.

Introduction

FULL-THICKNESS SKIN wounds are a major clinical burden in the United States both among military and civilian populations. About 500,000 patients are treated annually, and globally there are an estimated 11 million burn injuries per year.[1,2] The cost to treat these wounds approaches $2 billion per year in the United States alone.[3,4] The standard of care for full-thickness injuries includes autologous skin grafting, which allows wound coverage and closure and helps reduce scarring from full-thickness wounds.[4–6] However, autologous grafting requires sufficient volumes of skin harvest sites, and in burn patients the availability of donor sites can be limited by extensive skin loss.[7–9] Furthermore, the donor site often develops fibrotic scarring and contracture, resulting in significant morbidity.[10] Allographs have been used as an alternative graft source, but this approach is limited as long-term treatment option for many patients due to the requirement for immunosuppressive drugs.[11,12]

The inherent limitations of autografts and allografts have resulted in development of acellular dermal substitutes, composed of synthetic or natural scaffolds (e.g., Integra and Biobrane). Dermal substitutes have been shown to improve wound healing,[13,14] but result in suboptimal cosmetic outcomes, often require a second split thickness skin graft procedure, and are expensive. More complex biological skin substitutes (e.g., Apligraf®, Dermagraft®, StrataGraft®, and TransCyte®) have been developed by tissue engineers to deliver improved treatments for patients. In cultured constructs, fibroblasts are mixed in a collagen-based gel and matured over several days. Keratinocytes are then cultured on the superficial surface, after which the graft is raised to an air–liquid interface to encourage epidermal maturation. However, these and other bioengineered skin prototypes have substantial limitations: they contain only two cell types; they lack sweat and sebaceous glands, hair follicles, and pigmentation; and they may not stimulate revascularization and innervation.[15,16] Furthermore, collagen remodeling in wounds treated with these skin substitutes has not been sufficiently investigated. Since the ultimate goal of a skin graft is to regenerate authentic anatomy and functionality of native skin, there is a focused need to develop bioengineered skin with additional cell types and thus full collagen remodeling potential.

To meet the need for bioengineered skin, bioprinting techniques can be used to accurately engineer tissue substitutes with appropriate three-dimensional structural organization.[17–20] Our laboratory has demonstrated that bioprinting can effectively and precisely fabricate complex tissue structures in an automated manner.[21] We further bioprinted skin composed of two layers and two cell types, which successfully closed large full-thickness wounds.[22–24] As a next step, we have bioprinted skin using additional cell types to promote pigmentation (melanocytes), hair follicle formation (follicle dermal papillary cells [FDPCs]), neovascularization (endothelial cells), and immunomodulation (adipocytes). This work represents a significant advancement in skin tissue engineering and constitutes the most native-like skin construct engineered to date. However, prior studies have not determined the ability of bioprinted skin to recapitulate normal collagen remodeling *in vivo*. To fully realize the wound healing potential of these constructs, we must thoroughly characterize both epidermal barrier formation and collagen fiber maturity, organization, length, and width following implantation. Thus, the purpose of this study is to test the ability of bioprinted human skin to integrate, form an epidermal barrier, and recapitulate normal collagen remodeling in full-thickness wounds in mice.

Materials and Methods

Experimental design

This study was designed as a proof-of-concept validation of full-thickness skin bioprinting to be used as a graft for full-thickness wounds in a controlled laboratory setting. The sample sizes for the experiments were calculated using power analysis based upon our anticipated results (means and standard deviations [SDs]). The mouse studies were divided into 3 groups of 4 animals (nu/nu mice) in each treatment group (12 mice total); bioprinted skin, control hydrogel, and untreated wounds. Data collection was performed at predetermined time points, with bandage changes and sample collection as described below. Our study end points were defined to include improved wound closure, reepithelialization, and collagen remodeling as primary end points and healthy, mature skin formation assessed by histology as a secondary end point.

Cell isolation and culture

Six human skin cell types were used in the bioprinting process for generation of each skin layer: epidermis—human keratinocytes and human dark-melanocytes (Ratio—9:1); dermis—human dermal fibroblast, human follicle dermal papilla cells, and human dermal microvascular endothelial cells (HDMECs; ratio—6:1:1); and hypodermis—human preadipocytes. Human dermal fibroblasts, keratinocytes, and preadipocytes were isolated from human skin obtained from discarded tissue (Cell Culture Systems from Discarded Operating Room Tissue, IRB00007586) as described previously.[25–27] Keratinocytes, fibroblasts, and preadipocytes were obtained by isolation from human donor skin. Briefly, a piece of human skin ($\sim 3 \times 3$ cm) was washed thrice in Dulbecco's phosphate-buffered saline (DPBS; pH = 7.2) contained antibiotics: penicillin/streptomycin (P/S) solution, gentamycin, and amphotericin. The hypodermis was separated, minced into small pieces, and transferred to 50 mL conical tubes with 1 mg/mL type I collagenase (incubation 30–60 min, 37°C). After fermentation, minced tissue was poured through nylon mesh (0.45 μm), and preadipocytes were centrifuged and then resuspended in Dulbecco's modified Eagle's medium (DMEM) with fetal bovine serum (FBS) and P/S supplements. The epidermis and dermis were minced into small pieces (1×1 mm) and separated after overnight incubation in 1.2 U/mL of dispase grade II in RPMI 1640 medium. Both tissues were poured through nylon mesh separately, centrifuged, and resuspended in specific cell medium.

For epidermal cells, keratinocytes were isolated from adult human skin and were cultivated in keratinocyte serum-free medium (Gibco, Grand Island, NY) with pituitary bovine serum and epidermal growth factor (EGF) supplements (Gibco). Keratinocytes were passaged at 70% confluence, and cells of passage 4–6 were used for bioprinting. Melanocytes were purchased from PromoCell (Heidelberg, Germany)

and cultivated in melanocyte growth medium supplemented with SupplementMix (PromoCell). Melanocytes were passaged at 90% confluence with cells of passage 4–7 used for bioprinting.

For dermal cells, fibroblasts were isolated from adult human skin and cultured in DMEM with high glucose (HyClone) with FBS (HyClone) and P/S (Gibco) supplements. Fibroblasts were passaged at 100% confluence with cells of passage 4–6 used for bioprinting. HDMECs were purchased from PromoCell and cultured in Endothelial Growth Medium-2 supplemented with FBS, hydrocortisone, human fibroblast growth factor-basic (hFGF-b), vascular endothelial growth factor (VEGF), R3 insulin-like growth factor (R3-IGF), ascorbic acid, hEGF, gentamycin, and heparin (Lonza, Myersville, MD). HDMECs were passaged at a confluence of 90% with cells of passage 4–7 used for bioprinting. FDPCs were also purchased from PromoCell and cultured in Follicle Dermal Papilla Cell Growth Medium supplemented with Growth Medium SupplementMix (PromoCell). FDPCs were passaged at 90% confluence with cells from passage 4 to 8 used for bioprinting.

For hypodermal cells, preadipocytes were isolated from adult human skin and cultured in DMEM with low glucose (HyClone) supplemented FBS (HyClone) and P/S solution (Gibco). Preadipocytes were passaged at 100% confluence with cells from passage 4 to 8 used for bioprinting.

To confirm maintenance of cell specific markers following cell culture before bioprinting, immunocytochemistry was performed. Fluorescent visualization showed strong positivity and specific localization of markers for all cell types: keratinocytes, fibroblasts, and adipocytes showed positive cytoskeleton staining for pan-cytokeratin, vimentin, and keratin71, respectively (Supplementary Fig. S1). Adipocytes stained positively for the synthesized hormone adiponectin in their cytoplasm, melanocytes produced melanosomes containing the protein Mel5, and HDMEC had cell membrane-positive CD31 staining (Supplementary Fig. S1).

Bioink preparation

To generate a bioink that when printed formed a robust gel, the fibrin hydrogel was combined with gelatin, glycerol, and hyaluronic acid.[28] First, all hydrogel components were sterilized by gamma-irradiation. Glycerol (100ul/mL), gelatin (35 mg/mL), and hyaluronic acid (3 mg/mL) were then dissolved in serum-free, DMEM-High Glucose (Gibco) in a 50 mL conical tube at 37°C for 12 h. Fibrinogen (30 mg/mL) was added to the mixture and allowed to dissolve at 37°C for 4 h. Cells were then suspended in the fibrinogen-based bioink with 40 μg/mL of aprotinin (Sigma, St. Louis, MO) in three separate syringes to be used for bioprinting: Epidermis—Keratinocytes and Melanocytes; Dermis—Fibroblasts, FDPCs, and HDMECs; and Hypodermis—preadipocytes. Thrombin (Sigma-Aldrich) was dissolved in phosphate-buffered saline (PBS) to make a 20 IU/mL solution in preparation for crosslinking of the constructs after printing.

Skin bioprinting

In preparation for printing, epidermal, dermal, and hypodermal cells were suspended in separate fibrinogen bioinks at a density of 20 million cells per mL and placed on ice for 30 min. These were then loaded into the integrated tissue organ printer. The integrated tissue and organ printer (ITOP) is made up of multiple cartridges to individually deliver cell-laden hydrogels, an XYZ stage/controller, dispensing module, and a closed chamber described previously.[21] Briefly the three-axis stage system (Aerotech, Inc., Pittsburgh, PA) and controller (Aerotech, Inc.) were used to direct the printing paths during the bioprinting process. The dispensing module consisted of a pneumatic pressure controller (ML-808FXcom; Musashi Engineering, Inc., Tokyo, Japan), syringe (Musashi Engineering, Inc.), and 500 μm diameter nozzle (Musashi Engineering, Inc.). The temperature within the chamber was maintained by a temperature controller (ThermoTEC; EIC Solutions, Inc., Warminster, PA) and a humidifier (AOS 7146; AIR-O-SWISS, Widnau, Switzerland) enclosed in an acrylic chamber. Computer aided design and computer aided manufacturing (CAD/CAM) were used to design and produce living tissue constructs.

In the printing process, the cell-laden hydrogel was printed through a 500-μm metal nozzle at 60–90 KPa of air pressure. The printed skin grafts were cross-linked by adding a thrombin solution (20 UI/mL, T4648; Sigma-Aldrich) for 60 min at room temperature. The bioprinter was used to deposit three layers of a cell laden fibrin bioink to form a 3×3 cm biomimetic, bioprinted skin graft; first a bottom hypodermal layer, a second dermal layer, and a third epidermal layer. Acellular, hydrogel-only constructs were also printed using this same method to be used as vehicle controls and were also cross-linked by the addition of a thrombin solution (20 UI/mL, T4648; Sigma-Aldrich) for 60 min at room temperature. Samples were submerged in a mixed medium containing a 1:1:1:1:1:1 ratio of each cell specific medium, 20 μg/mL aprotinin, and P/S. Medium was changed every day for 4 days before being implanted onto full-thickness wounds.

Full-thickness wound creation, wound treatments, bandaging, and euthanasia

The ability of the bioprinted skin to deliver viable cells directly onto wounds and replace the missing hypodermis, dermis, and epidermis was evaluated by creating a 2.5×2.5 cm (L × W) full-thickness excisional wound on the back of 12 male athymic nude (Nu/nu) mice (Charles River Laboratories, Wilmington, MA). All animal procedures in this study were performed according to protocols approved by the Wake Forest University Health Sciences Animal Care and Use Committee (Optimization of Bioengineered Skin, A18-065).

The skin was cleaned with iodine and then sterilized with alcohol swaps. The animals were sedated and maintained under anesthesia using inhaled isoflurane through a nose cone. The wound borders were marked on the back of the mouse using a sterile marker and ruler. The full-thickness defect was then made by surgical removal using metzenbaum dissecting scissors. The animals in this study were divided into three groups of four animals in each treatment group and all the mice euthanized for evaluation after 3 weeks ($n = 4$). The first group did not receive a treatment, instead only a standard wound dressing was applied to cover the wounds (wound only), the second group received fibrin hydrogel-only bioprinted grafts (hydrogel only), and

the third group was treated with bioprinted skin (bioprinted skin). Hydrogel only and bioprinted skin grafts were engrafted into the wound site, tucked under any overlying mouse skin, and then sutured into the wound with 6-0 Prolene on the cranial, lateral, and caudal sides of the graft.

All groups were bandaged by applying a custom sized, nonadherent, nonabsorbent square Adaptic™ dressing (Acelity, San Antonio, TX), sutured in place at each corner with 4-0 Prolene. This was followed by a Tegaderm™ bandage (3M, St. Paul, MN). A custom gauze bolster bandage was then applied with surgical tape. The mice were monitored for postoperative recovery daily, and the wounds were inspected under isoflurane anesthesia twice each week to document the wound size, reepithelialization, and closure; to clean the mouse and administration of antibiotics; and for re-bandaging.

After 21 days the study was ended and the wound areas harvested. Animals were sedated with isoflurane for final imaging, followed by lethal overdose of isoflurane and cervical dislocation. Wounds were divided for histology, immunohistochemistry, and scanning electron microscopy analysis.

Digital planimetry

Digital photographs of the wounds were taken every 7 days for 3 weeks. The photographs were taken using a 12 megapixel lens and a sterile ruler. Digital images were then analyzed using standard methods.[29] Wound closure and epithelialization were measured using ImageJ to determine the area of open wound and epithelialization, which can be separated by the color and texture of the healing wound area (Supplementary Fig. S2). We determined open wounds as being shiny and dark red in color, while the epithelium had a generally matte/opaque with a pink or white color tone. Contraction was measured as the area inside the scarred edge at each time point, compared with the original open wound using ImageJ.

Histology

Sections of the wound samples were fixed for 48 h in 4% paraformaldehyde and then transferred to 70% ethanol before paraffin processing. A microtome (Leica) was used to generate 5 μm sections containing both the center and edge portions of the treated wounds. Slides were then stained with hematoxylin and eosin, Masson's trichrome, and picrosirius red for histology and imaged by light microscopy. The picrosirius red stained sections required an additional polarized filter for optimal imaging. Images were then examined to determine the degree of epidermal formation and extent of epithelialization, dermal organization, blood vessel formation, keratin staining, collagen staining, and evaluation of extracellular matrix composition and organization, compared with normal undamaged mouse and human skin sections.

Picrosirius red image analysis with MATLAB, CT-FIRE, and CurveAlign

Once picrosirius red images were captured, they were analyzed with the CT-FIRE (curvelet transform-fiber extraction) and CurveAlign programs, designed by the Laboratory for Optical and Computational Instrumentation, University of Wisconsin Madison.[30] Settings were kept at default, and data were input into MATLAB for analysis and graphing.[31] CT-FIRE was used to overlay each collagen fiber and then quantify individual fiber width and length ($\approx$300 fibers per image; 3 images per sample; 12 samples per group; >11,000 fibers per group). The resultant mean collagen fiber length in pixels, SD, and sample size were then statistically analyzed using GraphPad Prism software. Similarly, CurveAlign was used to overlay each collagen fiber, which was then converted into a direction heat map, allowing for quantification of the coefficient of alignment, with zero being no alignment (like uninjured skin collagen) and 1 being complete alignment (more scar like). Images were processed as $\approx$300 fibers per image; 3 images per sample; 12 samples per group; and >11,000 fibers per group. The coefficient of alignment for each group was then analyzed using GraphPad Prism software. In addition, collagen fiber color was quantified using a custom MATLAB code. Briefly, a color threshold was used to isolate the four main colors seen in picrosirius red stained samples under polarized light; red, orange, yellow, and green. This allowed for quantification of the relative percentage of each color by dividing the pixel count of each color by the total pixel count for each image (Supplementary Fig. S3).

Immunohistochemistry

Immunohistochemical (IHC) costaining with Lamin A+C and Pan-Cytokeratin was used to visualize integrated human cells and epidermal formation in the regenerating skin, respectively. Costaining with Mel5 and Pan-Cytokeratin was used to confirm the presence of melanin in relation to keratinocytes. Finally, CD146 was used to determine capillary formation. For IHC, the incubation time was performed at room temperature. Slides were warmed for 1 h at 60°C to ensure bonding to the slides. Antigen retrieval with proteinase K (Dako, Carpinteria, CA) was performed on all slides with incubation for 5 min. Sections were then permeabilized for 5 min using 0.05% Triton X-100 in PBS (PBST). Nonspecific antibody binding was minimized by incubating sections for 10 min in Protein Block Solution (Dako). Sections were incubated for 12 h at room temperature in a humidified chamber with primary antibodies from the following: Lamin A+C (catalog No. ab108595; Abcam, Cambridge, MA), Pan-Cytokeratin (IR053; Dako), Pan-Cytokeratin (PA1-27114; Invitrogen, Rockford, IL), Mel5 (HMB45; Dako), Adiponectin (MA1-054; Invitrogen), Vimentin (MA5-145; Invitrogen), and ZO-1 (MABT339; Millipore, Burlington, MA).

After the primary incubation, the slides were washed in tris buffered saline (TBS) for 5 min thrice. Sections were then incubated for 60 min with FITC anti-mouse (FI-2000; Vector Laboratories, Burlingame, CA) and Texas Red anti-rabbit (TI-1000; Vector Laboratories) secondary antibody solution at a 1:200 dilution. After washing, sections were incubated with DAPI (D3571; Life Technologies, Eugene, OR) at a 1:10,000 dilution for 5 min and then washed thrice in TBS for 5 min. Slides were cover slipped with ProLong™ Gold Antifade Mountain (Life Technologies). To control the staining process, negative controls were performed with primary antibody incubations and a blocking

solution incubation in place of the primary antibody. The negative controls demonstrated no immunoreactivity. All samples were imaged using a Leica DM4000B upright microscope with fluorescence at 647, 594, and 380 nm.

Scanning electron microscopy

To analyze the structure and morphology of the bioprinted skin, full-thickness samples were taken at 21 days postimplantation and fixed in glutaraldehyde (2.5% solution in DPBS, pH 7.4) overnight at +4°C. The samples were washed thrice in DPBS and, after dehydration in ethanol, were dried using a critical point dryer (Leica EM CPD300) for $\sim$1 h. Samples were cross-sectioned, immobilized on a stub, and coated with particles of gold-palladium using a sputter coater (Leica EM ACE600). The resulting replica was analyzed under a FlexSEM1000 scanning electron microscope (Hitachi).

Statistical analysis

Data for each experimental group were expressed as the mean $\pm$ SD and statistical significance determined using statistical analysis software (GraphPad Prism; GraphPad Software, Inc.). Mixed models analysis of variance was used to compare the results, including the factors TREATMENT, DAY, and TREATMENT $\times$ DAY interactions ($n=4$). For CT-FIRE collagen fiber analysis, histograms were constructed from 10000 data points or more, and the resultant mean collagen fiber lengths in pixels were analyzed. For CurveAlign, the coefficient of alignment, with 0 being no alignment and 1 being complete alignment, was measured from over 300 data points for each of 3 images for all 4 treatment groups.

Results

Full-thickness skin bioprinting

Extrusion bioprinting was used to fabricate square, multilayer biomimetic structures. A 3×3 cm square graft was printed through layer by layer bioink deposition. During printing, the gel was extruded from 500 μm metal nozzle as parallel hydrogel rods. Each rod was positioned with the centers 750 μm apart, resulting in a confluent bioink square. The hypodermal layer was first printed with rods oriented in the *x*-plane, followed by the dermal layer printed with rods oriented in the *x*-plane, and finally the epidermal layer printed with rods in the *y*-plane (Fig. 1B). The resulting bioprinted graft was tri-layer, 3×3 cm square graft with a thickness of $\sim$1 mm (Fig. 1D). Cell-laden bioprinted skin and four hydrogel-only control grafts were then matured for 4 days and then engrafted in full-thickness wounds on mice. The remaining bioprinted samples were fixed as described above and imaged using bright field microscopy. We found that the bioprinted skin was highly cellularized compared with the clear acellular, hydrogel-only constructs (Fig. 1E).

Wound treatment and product application

Full-thickness wounds with a consistent size and depth were created. Representative images of wounds and treatments are shown in Figure 1. Overall, both the bioprinted skin and hydrogel only constructs were able to be administered by a single surgeon with minimal preparation steps. Application of both products resulted in consistent and complete coverage of the wound area. Both the bioprinted skin and hydrogel only constructs were structurally stable enough to suture into the wound area, and most sutures remained in place for the entirety of the study. Bandaging occurred every 3–4 days, and wound images were taken. We found that the optimal bandaging technique was to apply a custom-sized, nonadherent, nonabsorbent square Adaptic dressing (Acelity), sutured in place at each corner with 4-0 Prolene. This was followed by a Tegaderm bandage (3M), and a custom gauze bolster bandage was applied with surgical tape as shown in Figure 1.

Full-thickness wound closure

Digital photographs were taken during each of the bandage change time points (days 0, 7, 14, 21) and assembled for each of the wounds (Fig. 2A). Gross morphology demonstrated that bioprinted skin treated wounds had complete closure at day 21, compared with open wounds in all other treatment groups. Epithelialization in the bioprinted skin treated group was confirmed through hematoxylin and eosin staining, which demonstrated complete wound closure and a stratified epithelium (Fig. 2B). Alternatively, the hydrogel only and untreated wounds only had sparse coverage and incomplete epithelialization.

Total wound closure

The percentage of open wound area relative to the original wound area was measured to quantify total wound closure at each time point (Supplementary Fig. S2). These measurements are shown combined and separately in Figure 3A and E, respectively. By day 7, wounds treated with bioprinted skin had a significantly greater percentage of total wound closure compared with the hydrogel only and wound only controls ($91.0\% \pm 7.3$ vs. $23.5\% \pm 18.0$, $19.9\% \pm 4.9$, respectively, $p<0.0001$). This trend continued at day 14, with bioprinted skin treated wounds all achieving complete closure ($100\% \pm 0.0$ vs. $64.1\% \pm 5.0$, $64.8\% \pm 13.9$, respectively, $p<0.0001$). By day 21, all wounds were above 70% total wound closure. Hundred percent of the bioprinted skin treated wounds had closed by day 21, compared with open wounds and incomplete closure in all untreated wounds and all wounds treated with the hydrogel only.

Wound contraction

For each time point, the outer visible wound border compared to the original wound area was quantified as the percentage wound contraction. These measurements are shown combined and separately in Figure 3B and E, respectively. All three groups showed consistent contraction up to 21 days, at which point there was no significant difference in contraction between bioprinted skin, control hydrogel, and wound only groups ($49.6\% \pm 20.3$, $53.8\% \pm 9.7$, $54.5\% \pm 12.4$, respectively, $p>0.05$).

Wound epithelialization

Epithelialization was defined visually as a matte appearing epithelial coating distinct from the dark red wound area and was measured at all time points. This was calculated by measuring the covered wound area within the contracted

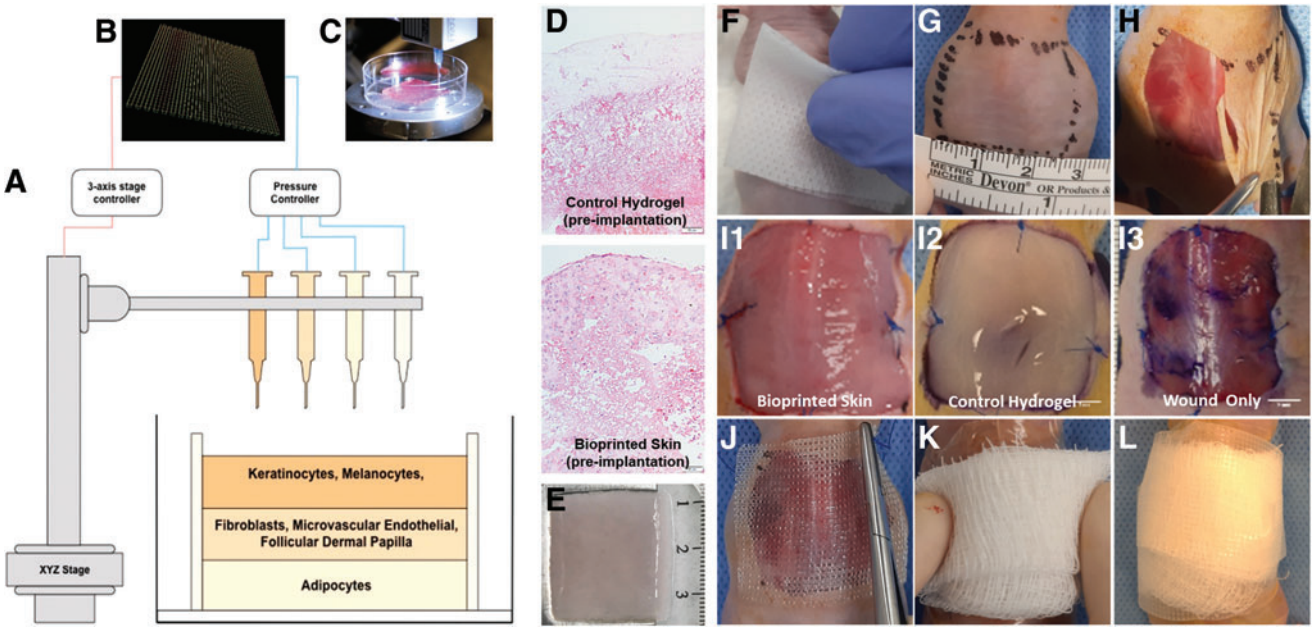

FIG. 1. Bioprinted skin fabrication, surgical method, and experimental groups. Diagram of the bioprinted CAD/CAM design, printing process, skin layers, and *in vitro* histology and a visual description of the steps involved in the preparation, wound creation, treatment administration, protective bolster bandaging of animals, and the treatment groups in this study. **(A)** The three-layer biomimetic skin design consists of a hypodermal layer (preadipocytes), a dermal layer (dermal fibroblasts and microvascular endothelial cells), and epidermal layer (keratinocytes and melanocytes), each printed using a separate syringe. **(B)** CAD/CAM design of the *square* graft consisted of parallel deposited rods 3 cm in length with a 90° rotation with each layer. **(C)** Bioprinting is performed in a sterile environment. **(D)** H&E staining of bioprinted skin confirms high cellularity, while the fibrin hydrogel only control graft is acellular. **(E)** The final product measures about 3×3 cm and is then allowed to crosslink in fibrin for 1 h. **(F)** The anesthetized mice were surgically prepped with isopropyl alcohol and betadine swabs. **(G)** The area for the excisional wound was marked with one 2.5×2.5 cm *square* drawn with sterile marker on the dorsum. **(H)** For the creation of the defect, the skin wound was created by removing 2.5×2.5 cm of full-thickness skin in the central back along the thoracic and lumbar area. **(I)** Wounds were immediately treated either with bioprinted skin **(I1)** or a fibrin hydrogel vehicle control **(I2)**; an additional group underwent no treatment **(I3)**. **(J)** The wound area was covered with an Adaptic™ dressing and sutured in place at the four corners. **(K)** The wound was then covered with a Tegaderm™ bandage, and a folded piece of gauze was placed on top. **(L)** Surgical tape was then used to attach the bandage to the wound area, forming a bolster dressing. CAD/CAM, computer aided design and computer aided manufacturing; H&E, hematoxylin and eosin. Color images are available online.

wound borders and representing it as a percentage of the original wound area. These measurements are shown combined and separately in Figure 3C and E, respectively. By day 7, wounds treated with bioprinted skin had a significantly greater percentage wound closure due to epithelialization compared with the hydrogel only and wound only controls ($83.6\% \pm 13.2$ vs. $1.5\% \pm 3.0$, $4.6\% \pm 9.3$, respectively, $p < 0.0001$). This trend continued at day 14 ($69.5\% \pm 22.7$ vs. $24.0\% \pm 10.1$, $17.0\% \pm 8.2$, respectively, $p < 0.001$). By day 21, epithelialization had contributed to over 30% of wound closure for all wounds, with a greater percentage of wound closure due to epithelialization on average in the bioprinted skin group compared with hydrogel and wound only controls ($50.4\% \pm 20.3$ vs. $34.6\% \pm 13.3$, $31.1\% \pm 7.8$, respectively, $p > 0.05$). To ensure that the epithelialization seen in the wound images correlated with true epidermal barrier formation, samples of the wound area were histologically processed and stained with hematoxylin and eosin (Fig. 2B). The hydrogel only and untreated wounds had sparse coverage and incomplete epithelialization only, compared with a thick stratified epidermis in wounds treated with bioprinted skin.

Combined analysis of wound area, contraction, and epithelialization

While crucial information is garnered by analyzing individual components of wound healing parameters (i.e., wound closure, contraction, and epithelialization), a combined analysis better illustrates the overall wound healing quality. This also allows for further understanding of the relative contributions of each wound healing parameter. To represent the combined wound healing analysis, we divided the healing wound into the percentage of wound area (red), percentage contraction (yellow), and percentage epithelialization (green) (Fig. 3E). Using this method of analysis, we can directly appreciate wound closure through the competing parameters of contraction and epithelialization for each treatment, thus highlighting the importance of both wound healing type and quality. We determined the best performing treatments by ranking them according to: (1) small open wound area, (2) least contraction, and (3) most epithelialization. Alternatively, the worst performing treatments had the opposite characteristics. Bioprinted skin treated wounds had the smallest wound area as the only group

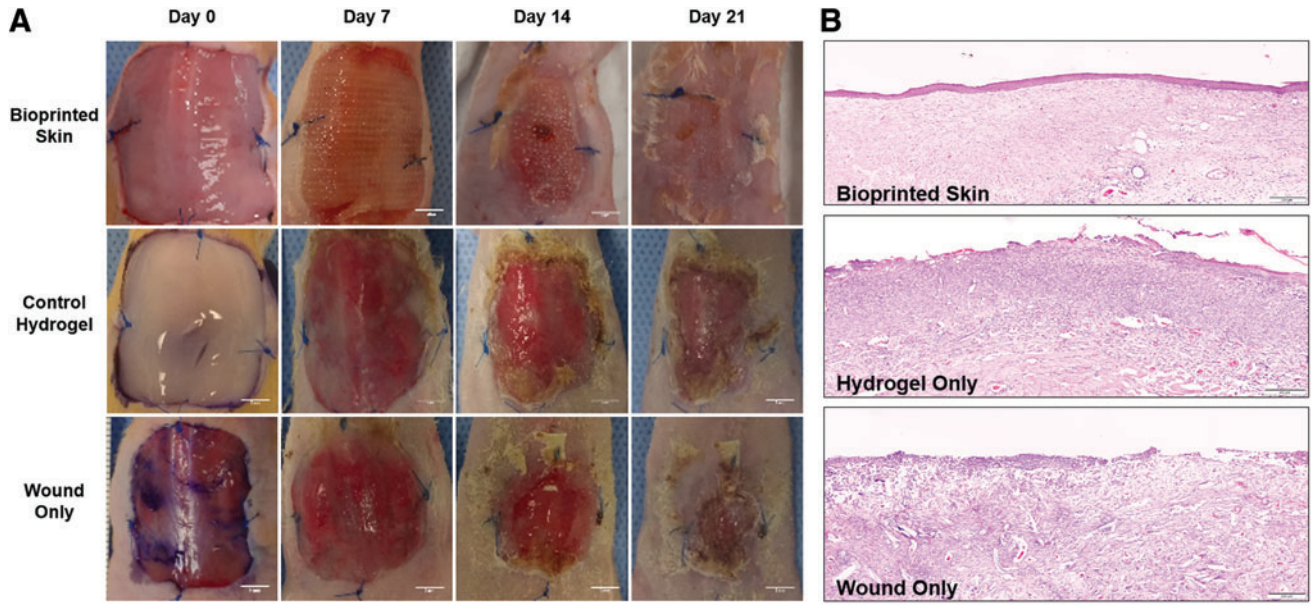

FIG. 2. Digital images of full-thickness wound closure over 21 days and H&E stained samples at day 21. **(A)** Digital photos were taken for each of the time points (days 0, 7, 14, 21) and compiled for each of the wounds. Gross morphology demonstrates accelerated wound closure time, and wounds were treated with bioprinted skin (images scaled to 3×3 cm; scale bar 5 mm). **(B)** Epithelialization in the bioprinted skin (*top*) was confirmed through H&E staining. The hydrogel only (*middle*) and untreated (*bottom*) wounds had only sparse coverage and incomplete epithelialization (stitched image at $20\times$ magnification; scale bar 200 μm; $n=4$). Color images are available online.

to have complete wound closure at the close of the study, the greatest amount of epithelialization, and the least contraction. However, contraction contributed to just under 50% of the overall wound closure. The hydrogel and wound-only groups had small open wounds at the end of the study, with less wound closure due to epithelialization and greater than half of wound closure due to contraction. Ultimately, the control hydrogel group performed slightly better in all categories than untreated wounds. Based on the combined analysis the order of best performance was (1) bioprinted skin, (2) hydrogel only control, and (3) wound only with standard bandaging.

Histological analysis

Sections stained with hematoxylin and eosin were evaluated to compare the overall composition and anatomical structure of each healing wound area. Representative images are shown in the first row of Figure 4. Healthy mouse and human skin were both used as controls for this analysis. The epidermis of normal skin tissue displayed the typical rete-peg protrusions into the dermis and a thick stratified epidermis. The mouse tissue also had visible hair follicle shafts. In comparing the wound histology showed that the bioprinted skin group had the most robust epidermal covering at the wound center, compared with granulation tissue in the control hydrogel and wound only groups. All groups had increased cellularity compared with normal tissue controls, suggesting increased inflammatory cells in the healing wound area. The bioprinted skin treated wounds had an immature appearing epidermis that laced rete-peg protrusions into the dermis with some stratification. Control hydrogel treated wounds had areas of maturing epidermis, but the wound center had no identifiable epidermis in most samples. The untreated wounds had inconsistent coverage, particularly at the days 14 and 21 time points, with a thinner epidermis in the areas of coverage. The dermis of healthy skin had organized fibers that were light pink in color, with hair follicles notably present in mouse skin. Bioprinted skin treated wounds also had light pink organized fibers in the dermis, as well as visible capillaries. The control hydrogel group has slightly less organized pink fibers in the dermis, while untreated wounds had a thick dermis with thin, purple disorganized fibers.

Masson's trichrome staining was performed to visualize keratin and collagen composition of the wounds. Trichrome staining helps identify extracellular matrix (ECM) components simultaneously (collagen stains blue; keratin stains red; cytoplasm stains pink; and nuclei stain brown). The second row of Figure 4 presents representative images of healthy mouse and human skin and the three treatment groups. Healthy skin had intense collagen staining (blue) in the dermis and intense keratin staining (red) in the epidermis. High cellularity was visible in the epidermis and dermis (brown nuclei). The bioprinted skin treated wounds also had intense keratin staining (red) with moderate collagen staining (blue), particularly deeper in the dermis, and high cellularity in the epidermis and dermis. Hydrogel treated wounds had faint keratin staining (red) with mostly cytosol staining instead of keratin (pink vs. red), slight collagen staining (blue), and high cellularity only in the dermis. Untreated wound tissues show highly disorganized and only faint collagen staining in the dermis (blue) with a disorganized epidermal layer with high cellularity (brown nuclei) and cytosol staining instead of keratin (pink vs. red).

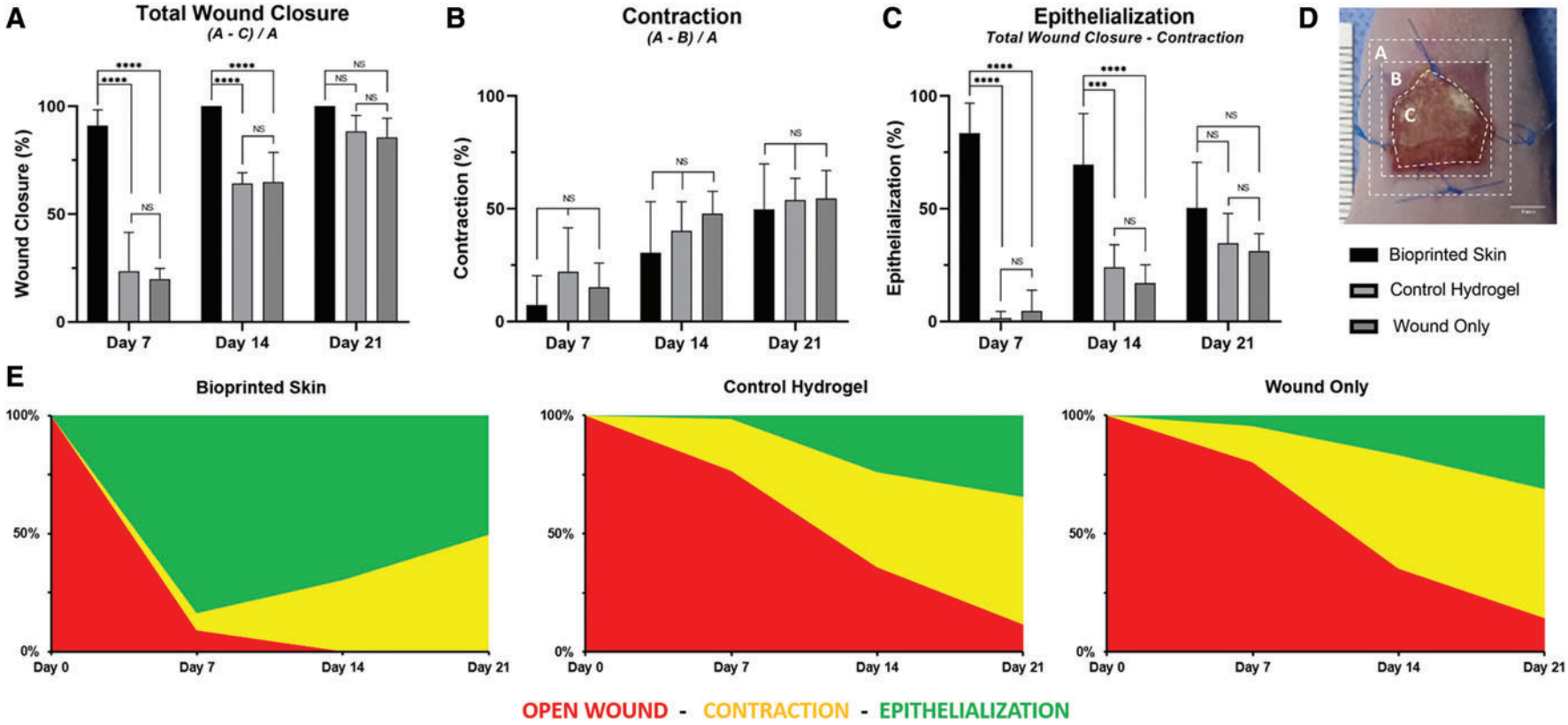

FIG. 3. Digital planimetry for total wound closure, contraction, and epithelialization. Individual plots for **(A)** total wound closure, **(B)** contraction, and **(C)** epithelialization over 21 days (****$p<0.0001$; ***$p<0.001$; NS, $p>0.05$, $n=4$). **(D)** The original wound area, outer healing wound border, and open wound area were measured for each treatment group at each time point using ImageJ. Total wound closure was calculated by subtracting the open wound area from the original wound area, divided by the original wound area [Total Wound Closure = (A − C)/A]. Contraction was calculated by subtracting the outer healing wound border from the original wound area, divided by the original wound area [Contraction = (A − B)/A]. Epithelialization was calculated by subtracting contraction from total wound closure (Epithelialization = Total Wound Closure − Contraction). The time to complete wound closure was quantified. **(E)** Combined wound healing analysis represents the total wound area at each time point divided into the percentage of wound area (*red*), percentage contraction (*blue*), and percentage epithelialization (*green*). With these analyses describing the healing wound over time, we can observe wound closure through competing parameters of contraction and epithelialization for each treatment. The best performing treatments were categorized as having the following: (1) small wound area, (2) least contraction, and (3) most epithelialization; the worst performing treatments had the opposing characteristics. Products are ranked from the best healing (*left*) to worst healing (*right*). Bioprinted skin had complete wound closure, greater epithelialization, and less contraction compared to hydrogel only and untreated wounds at day 21. Color images are available online.

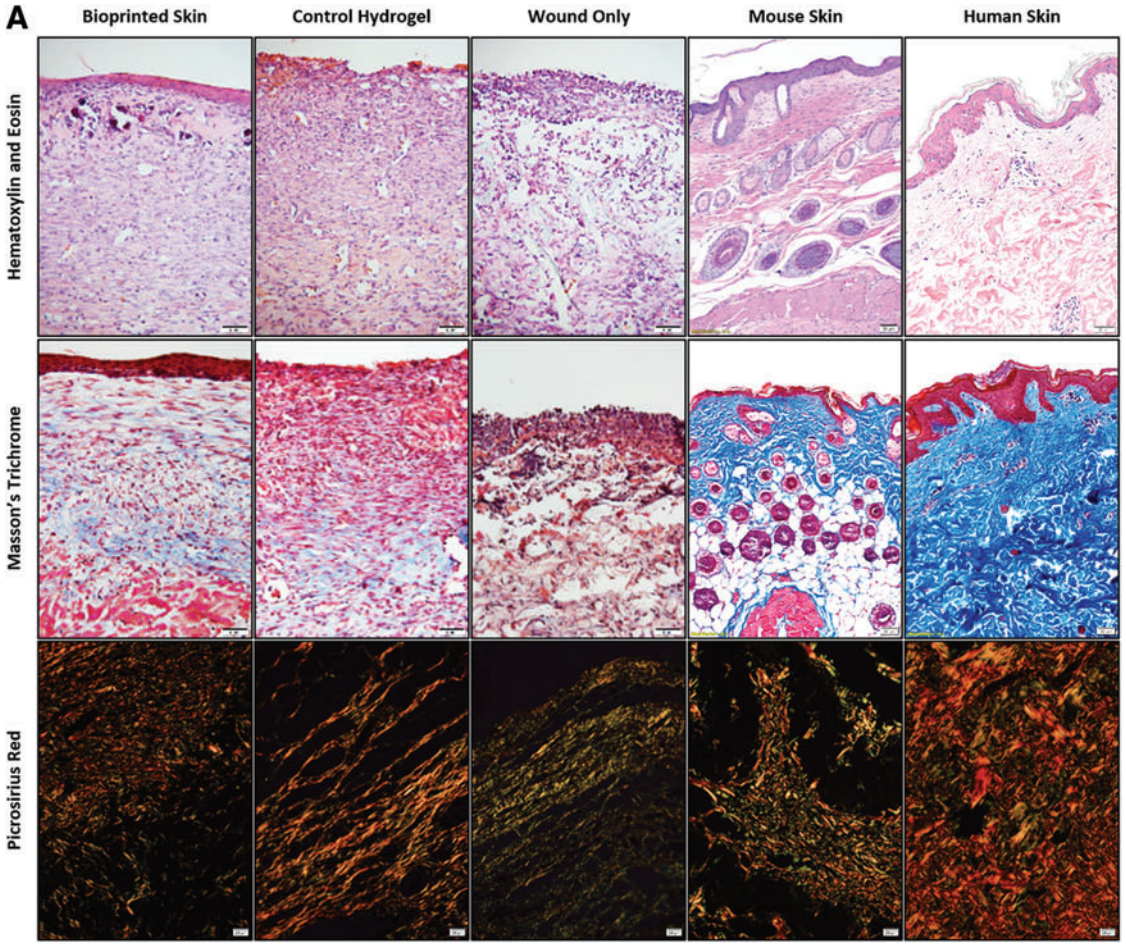

B

Histological Findings	Bioprinted Skin	Control Hydrogel	Wound Only
Epidermis Formation	++	-	-
Blood Vessel Formation	+++	++	+
Keratin Staining	+++	+	+
Collagen Staining	++	+	-
Collagen Fiber Orientation	Random	Parallel	Parallel

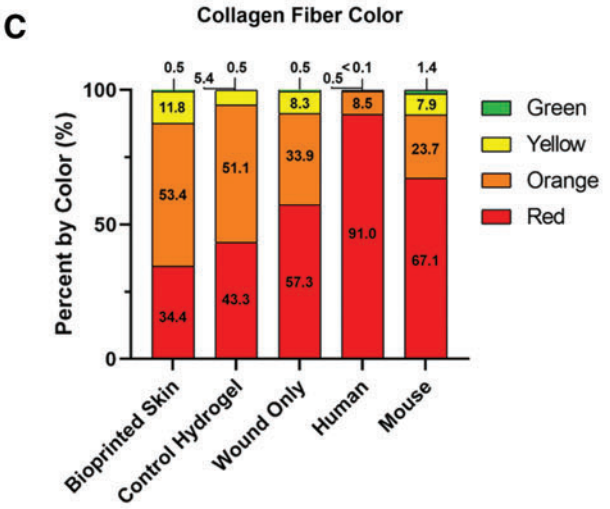

FIG. 4. Representative histological images for H&E, Masson's Trichrome, and Picrosirius Red. **(A)** Representative H&E stained histological images (*Row* 1; 20× magnification; scale bar 50 μm; $n=4$). Only the bioprinted skin group had developed an epidermis. Bioprinted skin-treated groups appear to have a dermis structure similar to healthy skin (thicker bundles, basket weave organization), while hydrogel only and untreated wounds had sparse or incomplete epidermis and a thick unorganized dermis. Representative Trichrome staining of tissues (*Row* 2; 20× magnification; scale bar 50 μm; $n=4$). Bioprinted skin showed the most similar staining intensity for keratin (*red*) and collagen (*blue*), compared to healthy skin. Hydrogel only treated wounds had some staining for keratin (*red*) and sparse dermal collagen staining (*blue*). Untreated wounds were highly disorganized, highly cellular (*brown*), and were not representative of healing skin. Representative Picrosirius Red staining of tissues viewed with polarizing light (*Row* 3; 20× magnification; scale bar 50 μm; $n=4$). Healthy skin is dominated by red mature collagen type I in a basket weave orientation. Bioprinted skin appeared most like healthy skin with this basket weave organized collagen fibers, while control hydrogel treated wounds had thick *orange* fibers organized in parallel, typical of scar formation. Untreated wounds appeared to show increased levels of immature *green* collagen type III fibers and were also organized more in parallel. **(B)** Summary table of histological findings. **(C)** MATLAB was used to quantify the relative percentage of each collagen color type by dividing the pixel count of each color by the total pixel count for each image, shown here as the average percentage for each treatment group ($n=4$). Color images are available online.

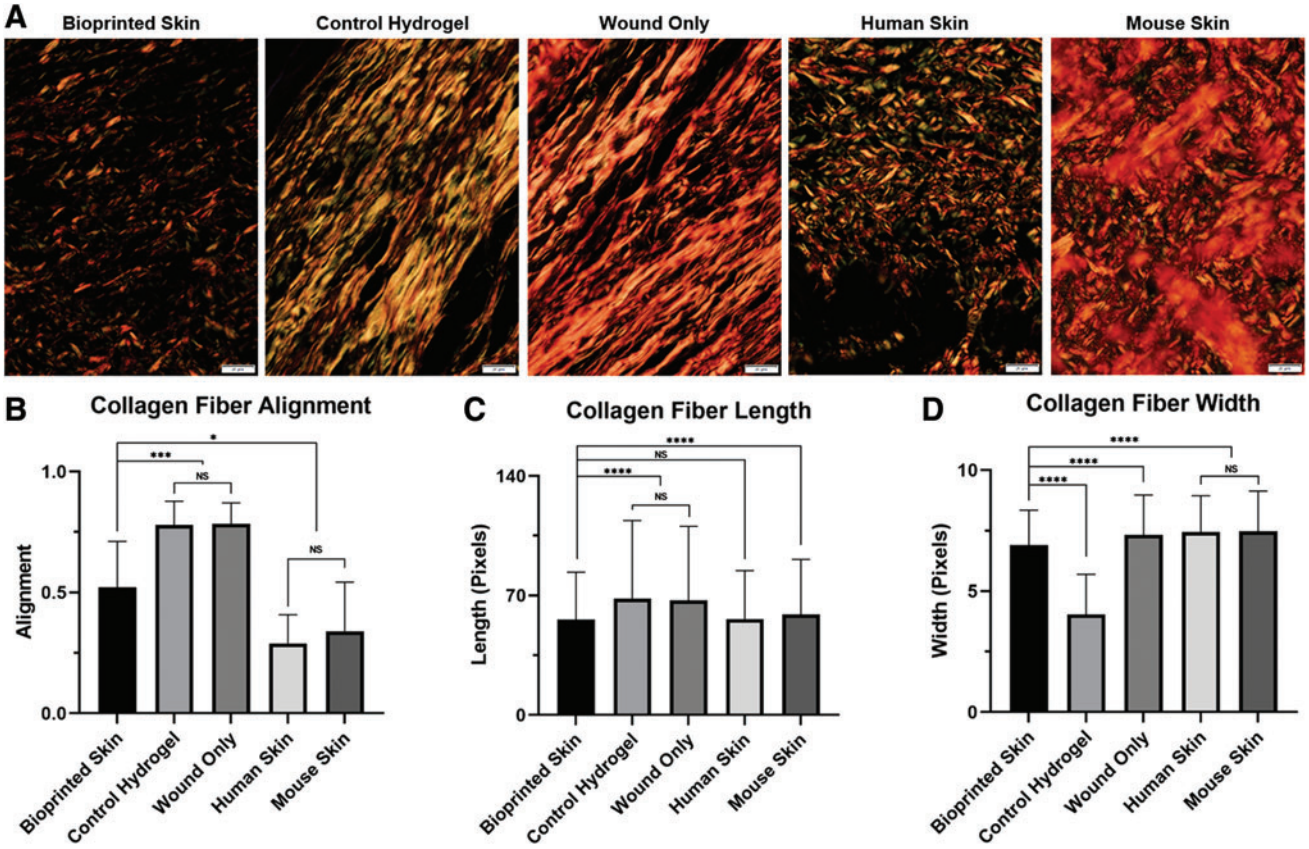

FIG. 5. Picrosirius Red analysis with CurveAlign and CT-FIRE to measure collagen fiber alignment, length, and width. **(A)** Representative picrosirius red stained histological images under polarized light (day 21, 40× magnification; scale bar 20 μm; $n=4$). **(B)** Collagen fiber alignment was measured using CurveAlign software and is represented as alignment, with zero being no alignment or more normal and 1 being complete alignment or more scar like (***$p<0.001$; *$p<0.05$; NS, $p>0.05$; $n>10{,}000$ fibers per group). Bioprinted skin had less aligned collagen fibers than the control hydrogel and wound only controls, but was more aligned than the human and mouse skin controls. **(C)** Collagen fiber length was measured using CT-FIRE software and is represented as length in pixels (****$p<0.0001$; NS, $p>0.05$; $n>10{,}000$ fibers per group). Bioprinted skin has similar collagen fiber length to bioprinted skin and was significantly shorter than mouse skin, control hydrogel, and wound only treatment groups. **(D)** Collagen fiber width was measured using CT-FIRE software and is represented as width in pixels (****$p<0.0001$; NS, $p>0.05$; $n>10{,}000$ fibers per group). Collagen in bioprinted skin was thinner than wound only samples, human skin, and mouse skin, but was significantly thicker than control hydrogel treated wounds. CT-FIRE, curvelet transform-fiber extraction. Color images are available online.

Picrosirius red staining can be viewed under polarized light to discriminate between mature and immature collagen. Immature collagen stains green/yellow (generally regarded as Collagen Type III), while organized and mature collagen fibers stain orange/red (generally regarded as Collagen Type I). Furthermore, collagen fiber orientation can be described as basket weave (normal, healing) or parallel (scarred, fibrotic). Row 3 of Figure 4 demonstrates representative images of healthy skin and the three treatment groups. Healthy skin demonstrated vibrant red and orange staining, indicative of an organized network of mature collagen fibers in a basket weave orientation. The bioprinted skin treated wounds were mostly composed of orange collagen fibers with both strong red and yellow staining, intermixed in a basket weave orientation, indicating normal healing. Alternatively, the control hydrogel group had long, thick collagen fibers, which were mostly orange and red. The collagen fibers were oriented in parallel, indicating fibrosis. This general pattern was also seen in the wound only group, with most collagen fibers also aligned in parallel.

Picrosirius red collagen fiber image analysis

Multiple methods were used to analyze collagen fiber color, alignment, length, and width to confirm the gross histological findings described above. First, we measured differences in collagen fiber maturity using a custom MATLAB code to measure the average percentage of each collagen fiber color in each treatment group (Fig. 4C). Bioprinted skin treated wounds had significantly less mature red fibers than both mouse and human skin ($34\% \pm 14.8$ vs. $91\% \pm 9.0$ and $67\% \pm 25.0$, respectively; $p<0.0001$). Alternatively, bioprinted skin was composed primarily of orange fibers (53.24 ± 10.3) and was most similar to control hydrogel treated wounds. Untreated wounds were most similar to mouse skin, both in terms of the number of red fibers ($57\% \pm 40.3$ vs. $67\% \pm 25.0$) and orange fibers ($34\% \pm 30.3$ vs. $24\% \pm 15.0$).

Next, CurveAlign was used to determine the coefficient of alignment of collagen fibers in each treatment group (Fig. 5B). Control hydrogel and wound only treated wounds

both had highly aligned collagen fibers (0.78 ± 0.10 vs. 0.79 ± 0.10, respectively; $p > 0.05$), typical of a parallel scar formation. Alternatively, normal human and mouse skin both had similarly unaligned collagen fibers (0.29 ± 0.12 vs. 0.34 ± 0.20, respectively; $p > 0.05$), typical of normal basket weave collagen fiber alignment. We found that bioprinted skin had less aligned collagen fibers than the control hydrogel and wound only controls (0.52 ± 0.19 vs. 0.78 ± 0.10 and 0.79 ± 0.10, respectively; $p < 0.001$), representing a more normal, basket weave collagen extracellular matrix. However, bioprinted skin treated wounds had greater alignment than normal human and mouse skin (0.52 vs. 0.29 ± 0.12 and 0.34 ± 0.20, respectively; $p < 0.01$), suggesting that ECM remodeling was not yet complete at 21 days in this model.

Finally, we further analyzed the picrosirius red images by quantifying the collagen fiber properties using CT-FIRE, a program designed by the Laboratory for Optical and Computational Instrumentation at the University of Wisconsin, which quantifies parameters of fiber length and width (Fig. 5C–D). Briefly, fibers are isolated from images by identifying edges (CT-FIRE algorithm and connecting those edges to segment total fibers). These segmented fibers are then analyzed to generate histograms of fiber parameters, such as angle, width, length, and straightness. When fiber length was measured, the control hydrogel and untreated controls had similarly long fibers (68.0 ± 45.9 vs. 67.2 ± 43.4, $p > 0.05$), typical of scar formation. Alternatively, bioprinted skin treated wounds had an average collagen fiber length that was significantly shorter and was most similar to normal human skin (55.9 ± 27.8 vs. 56.3 ± 28.3, $p > 0.05$) and was also shorter than mouse skin collagen fibers (55.9 ± 27.8 vs. 58.9 ± 32.23, $p < 0.0001$). These findings suggest that bioprinted skin promoted generation of collagen fibers of normal length for human skin. Finally, fiber width measurements showed that the bioprinted skin treated wounds were more narrow than normal human, mouse, and untreated wound skin (6.9 ± 1.5 vs. 7.4 ± 1.5, 7.5 ± 1.7, 7.3 ± 1.6, respectively; $p < 0.0001$). The fibers of bioprinted skin treated wounds were wider than control hydrogel treated wounds (6.9 ± 1.5 vs. 4.1 ± 1.7), suggesting greater maturity toward normal extracellular matrix formation.

Scanning electron microscopy

Scanning electron microscopy was used to analyze collagen fibrils and cell morphology of newly formed tissue in the full-thickness wound area of wounds 21 days post-treatment with bioprinted skin or control hydrogel only compared with a native mouse skin (Fig. 6). The epidermis of the bioprinted skin had uniform thickness and was composed of keratinized, stratified squamous epithelium, E1. Furthermore, the epidermal cell morphology of the bioprinted skin was comparable to native mouse skin (E3) with a clear stratum basale, stratum spinosum, stratum granulosum, and stratum corneum. Alternatively, the control hydrogel sample had sparse epidermal coverage with varying epidermal thickness along the area of the wound, with covered areas also represented by epithelial cells of all epidermal layers, E2. Even more significant differences were observed in the dermis. The bioprinted skin treated wounds formed extracellular matrix fibrils oriented with a normal, basket weave architecture (D1) similar to native mouse skin (D3), confirming our findings from picrosirius red imaging. Neo blood vessels were also present in the bioprinted skin treated wounds. Alternatively, control hydrogel treated wounds formed dermal extracellular matrix with collagen fibrils oriented in parallel (D2), typical of scar formation.

Immunohistochemistry

Pan-Cytokeratin and Lamin A+C stained sections were used to compare the epidermal structure and human cell integration. Pan-Cytokeratin stains epidermal keratinocytes, while lamin A+C is a human cell specific nuclear stain. Representative images are shown in the first column of Figure 7. In human skin, the stratified epidermis stained positively for Pan-Cytokeratin (green) and highlighted the rete-peg protrusions into the dermis. Lamin A+C staining was positive throughout the sample (red), with the highest concentration cells in the epidermis and moderate cellularity in the dermis. The bioprinted skin treated wounds also stained positively for Pan-Cytokeratin, but no rete-pegs were present in the wound area. In addition, Lamin A+C stained positively, confirming the integration of human cells into the wound area. However, Lamin A+C staining was only present in the dermis. Finally, control hydrogel treated wounds had only sparse Pan-Cytokeratin staining and no positive signal for Lamin A+C.

Mel5 and Pan-Cytokeratin stained sections were used to evaluate and compare melanin (green) production and melanocyte integration in relation to the epidermis (red). In human skin, Mel5 staining was found sparsely in the epidermis and scattered throughout the dermis. Similarly, Mel5 was found just below the epidermis and randomly throughout the dermis in the bioprinted skin treated group. Only faint staining for Pan-Cytokeratin was present in the hydrogel only group, with no signal present for Mel5.

Adiponectin and vimentin stained sections were used to evaluate and compare human dermal fibroblast (red) and preadipocyte (green) integration. In human skin, vimentin stained positively in a thin dermal area below the epidermis, while adiponectin stained a large hypodermal area. In wounds treated with bioprinted skin the entire dermal area stained positively for vimentin, but no adiponectin staining was present. The high number of human fibroblasts present in the dermis likely guided the normal collagen deposition described above. In the control hydrogel treated group there was only sparse staining for adiponectin and no staining for the highly human specific vimentin antibody.

ZO-1 and Pan-Cytokeratin stained sections were used to evaluate the presence of tight junctions (green) in relation to the epidermis (red). We found that ZO-1 staining highlighted blood vessel lumens on our stained samples. In human skin, ZO-1 staining was most pronounced deep in the hypodermal region. Alternatively, ZO-1 stained both in the superficial and deep in the dermis, with pronounced lumen in both areas. The control hydrogel treated wounds also had positive staining of ZO-1 in both the superficial and deep dermis; however, fewer blood vessel lumens were present.

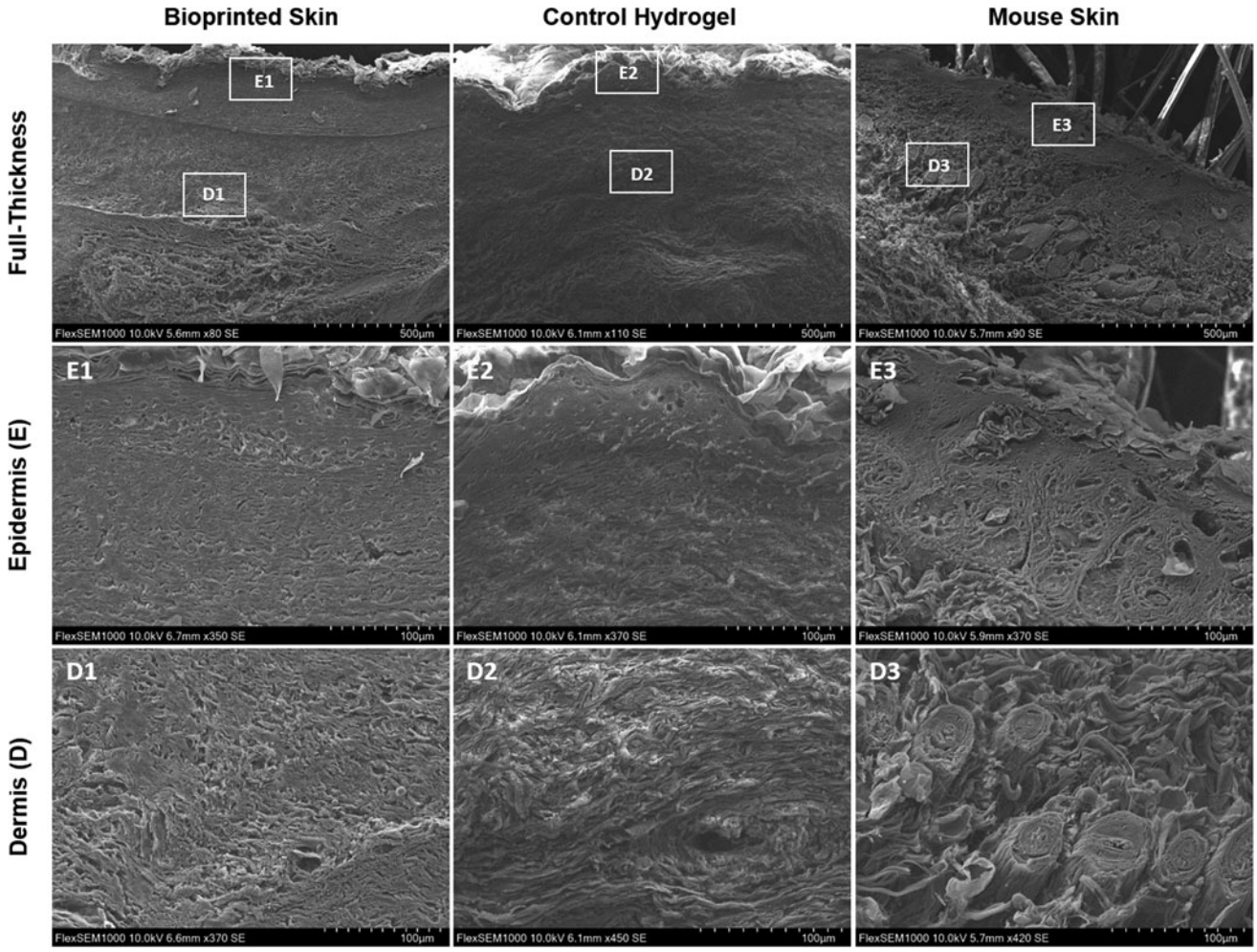

FIG. 6. Representative scanning electron microscopy images. Scanning electron microscopy images of bioprinted skin, control hydrogel, and mouse skin (*Row* 1 scale bar 500 µm; *row* 2 scale bar 100 µm; $n=4$). The bioprinted skin treated wounds displayed a unique separation in the dermis formed by the incorporated bioprinted skin in the wound area, with mouse epidermis healing over the top **(E1–E3)**. Dermal collagen in the bioprinted skin appeared to be in a normal, basket-weave orientation **(D1)** similar to normal mouse skin **(D3)**. Alternatively, the control hydrogel group had thick parallel collagen bundles in the dermis, typical of scar formation **(D2)**. These results confirm our findings with picrosirius red staining and quantification in Figure 6.

Discussion

This study demonstrated that bioprinted skin is easy to apply onto full-thickness wounds, integrates, forms an epidermal barrier, and recapitulates normal collagen remodeling in full-thickness wounds in mice. Histological analysis was used to support these observations, demonstrating that these treatments promote normal healing of these full-thickness wounds, resulting in the formation of an epidermal barrier and dermis with normal collagen ECM architecture.

Our wound morphometric analysis demonstrated increased epidermal coverage in wounds treated with bioprinted skin and was confirmed by histological staining of the tissues. Masson's trichrome staining demonstrated that bioprinted skin-treated wounds had a thicker epidermis with greater cellularity compared to untreated wounds. This was demonstrated with intense keratin staining, and this group was the most comparable to healthy skin; however, the epidermis lacked rete-peg formation. Conversely, untreated and control hydrogel treated wounds resulted in sparse epidermal covering, a thin epidermal layer, low cellularity, and weak keratin staining. These findings are typical of a less mature epidermis, suggesting that it is developing at a slower rate than the bioprinted skin treated wounds. In comparing the three groups, bioprinted skin was superior in accelerating closure and epithelialization, while all wounds had similar contraction. This is to be expected due to the cellularity of the bioprinted constructs guiding epidermal maturation. Ultimately, the wounds regenerated using bioprinted skin were able to heal faster and with mature and healthy epidermal coverage.

The dermal ECM quality and composition is essential for long-term engraftment and success of healing wounds.[32] The formation of healthy ECM facilitates normal mechanical and cellular properties. Alternatively, an abnormal ECM composition is typically present in scarring and contraction and is correlated with loss of mechanical strength

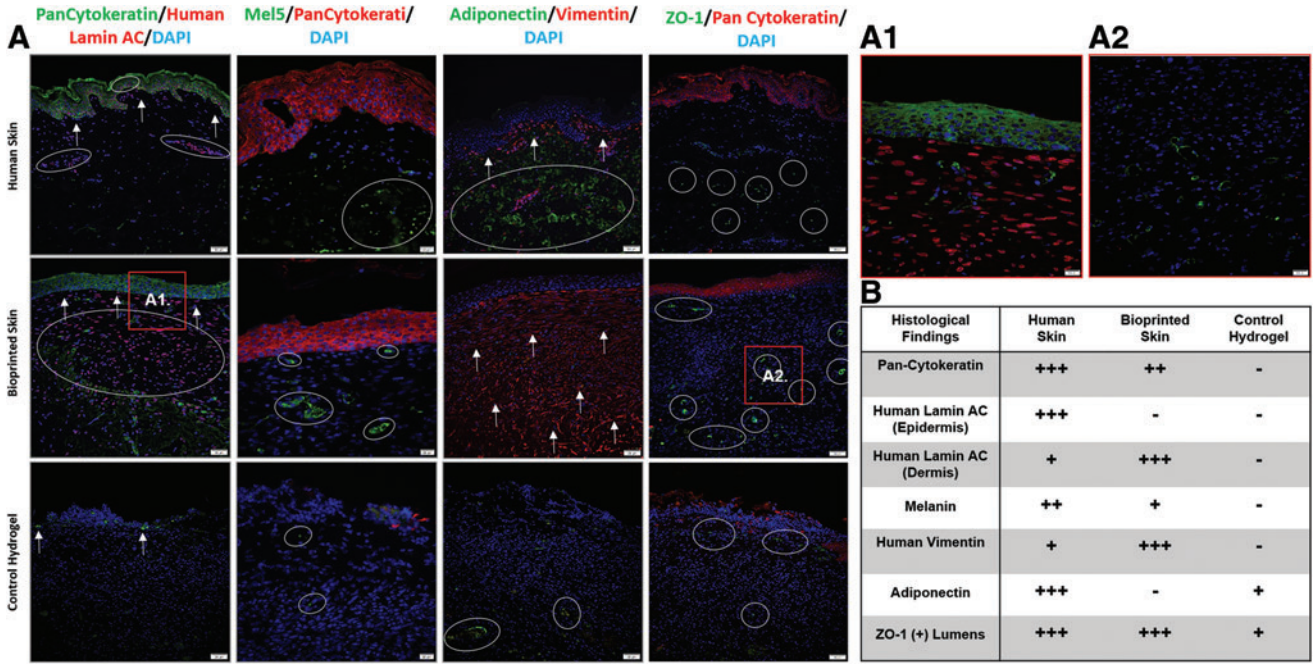

Histological Findings	Human Skin	Bioprinted Skin	Control Hydrogel
Pan-Cytokeratin	+++	++	-
Human Lamin AC (Epidermis)	+++	-	-
Human Lamin AC (Dermis)	+	+++	-
Melanin	++	+	-
Human Vimentin	+	+++	-
Adiponectin	+++	-	+
ZO-1 (+) Lumens	+++	+++	+

FIG. 7. Representative immunofluorescent images for Lamin A+C, Pan-Cytokeratin, Mel5, Adiponectin, and ZO-1. **(A)** Representative images of Pan-Cytokeratin (*green*) and Human Lamin A+C (*red*) immunofluorescent images (*Column* 1; 20× magnification; scale bar 50 μm; $n=4$). Bioprinted skin was the most like normal tissue, with a thick epidermis (*arrows*) and integrated human cells (*circles*, see also **A1**; 40× magnification; scale bar 20 μm; $n=4$), while the control hydrogel group only had sparse keratin staining in the epidermal region and no human cells. Representative images of Mel5 (*green*) and Pan-Cytokeratin (*red*) immunofluorescent images (*column* 2; 40× magnification; scale bar 20 μm; $n=4$). Bioprinted skin had some positive staining for Mel5 (*circles*) in both the superficial and deep dermis, while the control hydrogel group had little or no positive staining. Representative images of Adiponectin (*green*) and Vimentin (*red*) immunofluorescent images (*column 3*; 20× magnification; scale bar 50 μm; $n=4$). Bioprinted skin had intense staining for vimentin (*arrows*) in the dermis, but no positive adiponectin staining (*circles*), suggesting that preadipocytes in the bioprinted skin may have differentiated into fibroblasts. Control hydrogel treated wounds had no vimentin staining due to the high human specificity of the antibody, but there was some adiponectin staining deep in the dermis. Representative images of ZO-1 (*green*) and Pan-Cytokeratin (*red*) immunofluorescent images (*column* 4; 20× magnification; scale bar 50 μm; $n=4$). Bioprinted skin was the most like human skin, with ZO-1 (*circles*) staining highlighting vascular lumens throughout the dermis (see also **A2**; 40× magnification; scale bar 20 μm; $n=4$). The control hydrogel group also had positive staining, but the structures were less luminal in shape. **(B)** Summary table of histological findings. Color images are available online.

and elasticity.[33,34] Masson's trichrome and picrosirius red staining confirmed our initial observations, demonstrating that bioprinted skin-treated wounds had a dermal ECM composed of mature collagen fibers intermixed with immature fibers in a basket-weave orientation with staining intensities consistent with mature skin. These initial observations were confirmed through MATLAB, CurveAlign, and CT-FIRE analysis software, which demonstrated that bioprinted skin guided collagen remodeling with collagen fibers that were most similar to human skin in length and organized in a nonparallel basket weave matrix. Furthermore, the bioprinted skin-treated wounds contained a balanced ratio of green- and red-stained collagen fibers, representing a mixture of young and mature fibers, which would be expected in a newly regenerating wound. In contrast, the untreated and hydrogel only treated groups showed thick parallel fibers, which were more red in tone, all of which are characteristics of hypertrophic scars.[35]

Our bioprinting approach demonstrated a simplified, single step bioprinting method with multiple cell types, which could be improved to include additional cell types. IHC staining confirmed integration of human cells from the bioprinted skin and alludes to the impact these cells must have played in providing a normal wound collagen remodeling environment. While the bioprinted skin-treated wounds do form an epidermis, Lamin A+C staining of human nuclei was only positive in the dermis. This was unexpected considering that human keratinocytes made up such a large ratio of the bioprinted skin preimplantation. It is possible that the initial keratinocytes formed an epidermal layer, but were then replaced by migrating mouse keratinocytes from the wound border. Further studies to determine this mechanism are ongoing. Furthermore, preadipocytes were added into the constructs to help modulate the immune response and improve vascularization. By day 21, there was no notable signal for adiponectin, while there was a strong and dense response for vimentin. This may suggest that preadipocytes differentiated toward fibroblasts once placed in the wound. Ultimately, it was likely that this large contingency of fibroblasts was responsible for laying down the normal, basket weave collagen extracellular matrix. Finally, ZO-1 staining highlighted the increased number of capillary lumens present in the bioprinted skin wound center compared with control hydrogel treated wounds. The increase in

capillaries would have allowed for increased delivery of endogenous immune cells, growth factors, and cytokines.

While melanocytes were engineered to contribute to pigmentation of healing wounds in mice treated with bioprinted skin, there was no notable pigmentation in the wound areas grossly. However, Mel5 confirmed an increased amount of melanin relative to nontreated and wound only groups. FDPCs were included in the bioprinted skin to help promote hair follicle formation, but no human hair follicles were present at day 21. Recent advances by Christiano and colleagues have demonstrated the feasibility of adding hair follicle spheroids into molded skin constructs, which could improve hair formation in our bioprinted skin design.[36,37] Further studies investigating pigmentation and hair follicle formation, as well as further characterization of the cellular components of bioprinted skin, both *in vitro* and *in vivo*, are ongoing.

There are some future directions and limitations to address with this study. First, this study had only one time point (day 21) for wound histological analysis. This was a useful time point for measuring differences in wound closure between bioprinted skin treated wounds and controls; however, it will be necessary to evaluate wounds within the first days of treatment following full-thickness wound formation to confirm epithelialization and assess the earliest wound healing events and the acute inflammatory response. Furthermore, it would be valuable to evaluate wound healing after a period of several months' postwound closure to evaluate late stage events such as scarring and continued tissue development, respectively. In addition, this study was performed in nude mice, reducing the concern of an immune rejection by the host. The next step will be to test the use of human cells to treat full-thickness wounds in a porcine model. Further studies will be required to evaluate the immune response, among various inflamed wound scenarios (diabetic sound, burns, infection, etc.) and in fully immunocompetent animals. For clinical translation, improved cell isolation and scale up of cell manufacturing techniques will be required to allow for a feasible method or production for an autologous product. To this end, less immunoresponsive or even immunosuppressive hydrogels that could reduce the contraction seen in this study could be utilized. Furthermore, future studies will be required to test the effectiveness of these products in other time frames and clinically relevant wound types.

Conclusion

We have demonstrated the ability of bioprinted skin to enhance closure of full-thickness wounds through epithelialization and normal collagen remodeling. To our knowledge, this article is the first to quantify collagen remodeling by bioprinted skin in full-thickness wounds. Bioprinted skin accelerated full-thickness wound closure by promoting epidermal barrier formation, without increasing contraction. Histological analysis demonstrated that human cells from the bioprinted skin integrated and that the wound formed an epidermal barrier and extracellular matrix most similar to native healthy skin. This healing process is associated with human cells from the bioprinted skin laying down a healthy, basket-weave collagen network. The remodeled skin is phenotypically similar to human skin and composed of a composite of graft and infiltrating host cells. Our methods and results can be used to guide further investigation of collagen remodeling by tissue engineered skin products to improve ongoing and future bioprinting skin studies. Ultimately, our skin bioprinting technology could translate into a new treatment for full-thickness wounds in human patients with the ability to recapitulate normal collagen remodeling in full-thickness wounds.

Acknowledgments

The authors Dr. Michael Seeds for article review and Dr. Mahesh Devarassety for technical support with MATLAB, CT-FIRE, and CurveAlign software.

Disclosure Statement

No competing financial interests exist.

Funding Information

Funding for this research was provided in part by the U.S. Army Medical Research and Development Command (USAMRDC) through the Medical Technology Enterprise Consortium (MTEC) (Grant No. W81XWH-19-9-001 [S.S.]) and NIH/NIAMS 1 F30 AR074866-01A1 (A.M.J).

Supplementary Material

Supplementary Figure S1
Supplementary Figure S2
Supplementary Figure S3

References

1. American Burn Association. Burn incidence fact sheet. 2018. http://ameriburn.org/who-we-are/media/burn-incidence-fact-sheet (accessed November 8, 2019).
2. Peck, M.D. Epidemiology of burns throughout the world. Part I: distribution and risk factors. Burns **37,** 1087, 2011.
3. Bickers, D.R., Lim, H.W., Margolis, D., *et al.* The burden of skin diseases: 2004 a joint project of the American Academy of Dermatology Association and the Society for Investigative Dermatology. J Am Acad Dermatol **55,** 490, 2006.
4. Kurd, S.K., Hoffstad, O.J., Bilker, W.B., and Margolis, D.J. Evaluation of the use of prognostic information for the care of individuals with venous leg ulcers or diabetic neuropathic foot ulcers. Wound Repair Regen **17,** 318, 2009.
5. Jeschke, M.G., Shahrokhi, S., Finnerty, C.C., Branski, L.K., and Dibildox, M. Wound coverage technologies in burn care: established techniques. J Burn Care Res **34,** 612, 2013.
6. Singh, M., Nuutila, K., Kruse, C., Robson, M.C., Caterson, E., and Eriksson, E. Challenging the conventional therapy: emerging skin graft techniques for wound healing. Plast Reconstr Surg **136,** 524e, 2015.
7. Herskovitz, I., Hughes, O.B., Macquhae, F., Rakosi, A., and Kirsner, R. Epidermal skin grafting. Int Wound J **13(Suppl 3),** 52, 2016.
8. Sun, B.K., Siprashvili, Z., and Khavari, P.A. Advances in skin grafting and treatment of cutaneous wounds. Science **346,** 941, 2014.
9. Boyce, S.T., Kagan, R.J., Greenhalgh, D.G., *et al.* Cultured skin substitutes reduce requirements for harvesting of skin autograft for closure of excised, full-thickness burns. J Trauma **60,** 821, 2006.

10. Robson, M.C., Barnett, R.A., Leitch, I.O., and Hayward, P.G. Prevention and treatment of postburn scars and contracture. World J Surg **16,** 87, 1992.
11. Yang, S.-X., Gao, H.-L., Xie, S.-S., Zhang, W.R., and Long, Z.-Z. Immunosuppression of triptolide and its effect on skin allograft survival. Int J Immunopharmacol **14,** 963 1992.
12. Burke, J., Quinby, W., Bondoc, C., Cosimi, A., Russell, P., and Szyfelbein, S. Immunosuppression and temporary skin transplantation in the treatment of massive third degree burns. Ann Surg 1**82,** 183, 1975.
13. Lesher, A.P., Curry, R.H., Evans, J., *et al.* Effectiveness of Biobrane for treatment of partial-thickness burns in children. J Pediatr Surg **46,** 1759, 2011.
14. Rahmanian-Schwarz, A., Beiderwieden, A., Willkomm, L.-M., Amr, A., Schaller, H.-E., and Lotter, O. A clinical evaluation of Biobrane® and Suprathel® in acute burns and reconstructive surgery. Burns **37,** 1343, 2011.
15. MacNeil, S. Progress and opportunities for tissue-engineered skin. Nature **445,** 874, 2007.
16. Nyame, T.T., Chiang, H.A., Leavitt, T., Ozambela, M., and Orgill, D.P. Tissue-engineered skin substitutes. Plast Reconstr Surg **136,** 1379, 2015.
17. Koch, L., Deiwick, A., Schlie, S., *et al.* Skin tissue generation by laser cell printing. Biotechnol Bioeng **109,** 1855, 2012.
18. Lee, W., Debasitis, J.C., Lee, V.K., *et al.* Multi-layered culture of human skin fibroblasts and keratinocytes through three-dimensional freeform fabrication. Biomaterials **30,** 1587, 2009.
19. Lee, V., Singh, G., Trasatti, J.P., *et al.* Design and fabrication of human skin by three-dimensional bioprinting. Tissue Eng Part C Methods **20,** 473, 2014.
20. Michael, S., Sorg, H., Peck, C.T., *et al.* Tissue engineered skin substitutes created by laser-assisted bioprinting form skin-like structures in the dorsal skin fold chamber in mice. PLoS One **8,** e57741, 2016.
21. Kang, H.W., Lee, S.J., Ko, I.K., Kengla, C., Yoo, J.J., and Atala, A. A 3D bioprinting system to produce human-scale tissue constructs with structural integrity. Nat Biotechnol **34,** 312, 2016.
22. Skardal, A., Mack, D., Kapetanovic, E., *et al.* Bioprinted amniotic fluid-derived stem cells accelerate healing of large skin wounds. Stem Cells Transl Med **1,** 792, 2012.
23. Binder, K.W., Zhao, W., Aboushwareb, T., Dice, D., Atala, A., and Yoo, J.J. In situ bioprinting of the skin for burns. J Am Coll Surg **211,** S76, 2010.
24. Albanna, M., Binder, K.W., Murphy, S.V., *et al.* In situ bioprinting of autologous skin cells accelerates wound healing of extensive excisional full-thickness wounds. Sci Rep **9,** 1856, 2019.
25. Yamada, S.S. Preparation of human epidermal keratinocyte cultures. Curr Protoc Cell Biol Chapter 2, Unit 2.6, 2004.
26. Takashima, A. Establishment of fibroblast cultures. Curr Protoc Cell Biol Chapter 2, Unit 2.1, 2001.
27. Carswell, K.A., Lee, M.J., and Fried, S.K. Culture of isolated human adipocytes and isolated adipose tissue. Methods Mol Biol **806,** 203, 2012.
28. Lee, S.J., Broda, C., Atala, A., and Yoo, J.J. Engineered carrtilage covered ear implants for auricular cartilage reconstruction. Engineered cartilage covered ear implants for auricular cartilage reconstruction. Biomacromolecules **12,** 306, 2011.
29. Molnar, J.A., Lew, W.K., Rapp, D.A., *et al.* Use of standardized, quantitative digital photography in a multicenter Web-based study. Eplasty **9,** e4, 2009.
30. Bredfeldt, J.S., Liu, Y., Pehlke, C.A., *et al*. Eliceiri, computational segmentation of collagen fibers from second-harmonic generation images of breast cancer. J Biomed Opt **19,** 016007, 2014.
31. Devaraseey, M., Skardal, A., Cowdrick, K., Marini, F., and Soker, S. Bioengineered submucosal organoids for *in vitro* modeling of colorectal cancer. Tissue Eng Part A **23,** 1026, 2017.
32. Midwood, K.S., Williams, L.V., and Schwarzbauer, J.E. Tissue repair and the dynamics of the extracellular matrix. Int J Biochem Cell Biol **36,** 1031, 2004.
33. Aarabi, S., Bhatt, K.A., Shi, Y., *et al.* Mechanical load initiates hypertrophic scar formation through decreased cellular apoptosis. FASEB J **21,** 3250, 2007.
34. Reilly, G.C., and Engler, A.J. Intrinsic extracellular matrix properties regulate stem cell differentiation. J Biomech **43,** 55, 2010.
35. Ehrlich, H.P., Desmoulière, A., Diegelmann, R.F., *et al.* Morphological and immunochemical differences between keloid and hypertrophic scar. Am J Pathol **145,** 105, 1994.
36. Higgins, C.A., Chen, J.C., Cerise, J.E., Jahoda, C.A., and Christiano, A.M. Microenvironmental reprogramming by three-dimensional culture enables dermal papilla cells to induce de novo human hair-follicle growth. Proc Natl Acad Sci U S A **110,** 19679, 2013.
37. Abaci, H.E., Coffman, A., Doucet, Y., *et al.* Tissue engineering of human hair follicles using a biomimetic developmental approach. Nat Commun **9,** 5301, 2018.

Address correspondence to:
Adam M. Jorgensen, BS
Wake Forest Institute for Regenerative Medicine
Wake Forest School of Medicine
Richard H. Dean Biomedical Building,
391 Technology Way
Winston-Salem, NC 27101

E-mail: ajorgens@wakehealth.edu

Shay Soker, PhD
Wake Forest Institute for Regenerative Medicine
Wake Forest School of Medicine
Richard H. Dean Biomedical Building,
391 Technology Way
Winston-Salem, NC 27101

E-mail: ssoker@wakehealth.edu

Received: November 20, 2019
Accepted: December 12, 2019
Online Publication Date: January 27, 2020